EUSIPCO 2013 1569743687

THEORETICAL INSIGHTS INTO THE PHASE RECTIFIED AVERAGING METHOD AND APPLICATION TO HRV ANALYSIS

Meryem JABLOUN, Philippe RAVIER and Olivier Buttelli

Université d'Orléans, FRANCE.
Institut PRISME, équipe signal pour les systèmes, 12 rue de Blois, BP 6744, 45067 Orléans, France.
E-mail addresses: firstname.lastname@univ-orleans.fr, URLs: www.univ-orleans.fr/prisme

ABSTRACT

Heart rate variability (HRV) signals are processed using the new time-frequency representation (PRSA-TFR) defined based on the Phase-Rectified Signal Averaging (PRSA) method. PRSA is a technique which enhances quasi-periodic components in nonstationary signals and thus improves frequency estimation. The PRSA-TFR is obtained by applying the PRSA method to sliding windows along univariate signals. Our aim is to characterize the deviation of PRSA-TFR of HRV signals during supine and tilt position from that of white Gaussian noise. This deviation can be used as a new tool to quantify the changes in sympathovagal balance without needing to predetermine fixed spectral boundaries.

First, we derive the probability density function of the energy distributed in the PRSA-TFR for a white Gaussian noise. Then, the Battacharya distance is used to evaluate the deviation of HRV PRSA-TFR from that of a Gaussian noise. The HRV PRSA-TFR deviation is assessed separately for supine and tilt positions. Synthetic and real HRV signals of short-term recordings are analyzed based on this new tool. The obtained results are compared with those obtained with a classical spectral method.

1. INTRODUCTION

The dynamics of Heart Rate Variability (HRV) which can be evaluated by analyzing the oscillations of the RR intervals of electrocardiograms are significantly sensitive to positions, emotion and fatigue [1, 2, 3]. They are related to the autonomic nervous system acting and influenced by both the sympathetic and parasympathetic branches. The analysis of the heart rate fluctuations can yield useful information for sportive medicine. In recent years, several theoretical and empirical research papers, related to the processing and analysis of HRV time-series, have been published [2, 3, 4, 5, 6, 7, 8].

In the current paper, our main contribution is to characterize univariate HRV time-series using the new time-frequency representation (PRSA-TFR) [9] derived from the Phase-Rectified Signal Averaging (PRSA) method [10]. PRSA is a technique recently introduced to enhance quasi-periodic components in nonstationary signals. We explore the ability of this method to capture the local periodicities and to improve the estimation of the frequency components underlying their time-evolution. The discrete time-series are processed using short-time sliding windows, the length of which is chosen convenient to capture low and high frequency ranges. In each time window, the PRSA is evaluated and the PRSA spectrum is obtained. Hence, a PRSA-TFR is defined in analogy with the spectrogram [9]. In this way, the time evolution of the most relevant frequencies is captured.

We demonstrate that the PRSA-TFR behavior of the HRV data during supine and tilt positions is different from that of independent, identically distributed (iid) Gaussian noise. This is established by theoretically deriving the probability density function (pdf) of the energy distributed in the PRSA-TFR for iid Gaussian noise. Then, we use the Battacharya distance to evaluate the deviation of the PRSA-TFR pdf of the HRV time-series from that of iid Gaussian noise.

This deviation can be used as a new tool to quantify the changes in sympathovagal balance without needing to predetermine fixed spectral boundaries. Actually, to assess the sympatovagal balance, classical spectral analysis methods of HRV signals need fixed low frequency (LF) and high frequency (HF) band ranges, and to date no reliable methods for the appropriate selection of frequency ranges is proposed even if a Task Force attempt [3] was made for a boundary standardization. Indeed, different frequency ranges occur in the literature [11] and these unstable frequency limits can be explained by individual ranges which can strongly be affected by physiologic conditions (health, physical activity, breathing, gender, aging, body position, breathing frequency, etc).

This paper is organized as follows. The principle of PRSA and PRSA-TFR are described and the pdf of PRSA-TFR for an iid Gaussian noise is derived in Section 2. The HRV data set and the Battacharya distance are summarized in Section 3 and Section 4 respectively. Results and discussions are presented in Section 5 for synthetic and real HRV time-series. The final section concludes with a summary and some perspectives on our study.

2. PRSA AND TIME-FREQUENCY REPRESENTATION

2.1 A short introduction to PRSA

When applied to a discrete time signal y, the PRSA method helps enhance existing quasi-periodic components in this signal when they are corrupted by artifacts and noise. The basic idea of PRSA is the averaging of segments of y. These segments are symmetric regarding to so-called anchor points, samples at which the instantaneous phase of the signal is close to zero. Therefore, the averaging process removes correlated or nonperiodic components of the signal (such as noise and artifacts) while the quasi-periodic components are enhanced.

In the following, the simplest version of PRSA is described [10]. The steps of the PRSA method are illustrated in Fig.1. The anchor points correspond to the increases in the signal y (Fig.1(b)), i.e. instants n such that

$$y_n > y_{n-1}. \tag{1}$$

Assuming a total of M anchor points indexed by n_m, $m = 1,\ldots,M$, segments of length $2L+1$ are centered on these anchor points (Fig.1(c-e)),

$$[y_{n_m-L}, y_{n_m-L+1}, \ldots, y_{n_m}, \ldots, y_{n_m+L-1}, y_{n_m+L}]. \qquad (2)$$

All these segments are averaged, which leads to the PRSA signal $\tilde{y}_\ell$

$$\tilde{y}_\ell = \frac{1}{M}\sum_{m=1}^{M} y_{n_m+\ell}, \quad \text{for } \ell = -L, -L+1, \ldots, L. \qquad (3)$$

The 'PRSA transform' $\tilde{Y}_q$ is obtained by evaluating the discrete Fourier transform (DFT) of the PRSA signal (3)

$$\tilde{Y}_q = \sum_{\ell=0}^{2L} \tilde{y}_{\ell-L}\ e^{-j2\pi\frac{q}{Q}\ell}, \quad \text{for } q = 0,1,\ldots,Q-1, \qquad (4)$$

where $\frac{q}{Q}$ is the discrete frequency and Q is the number of samples in the DFT.

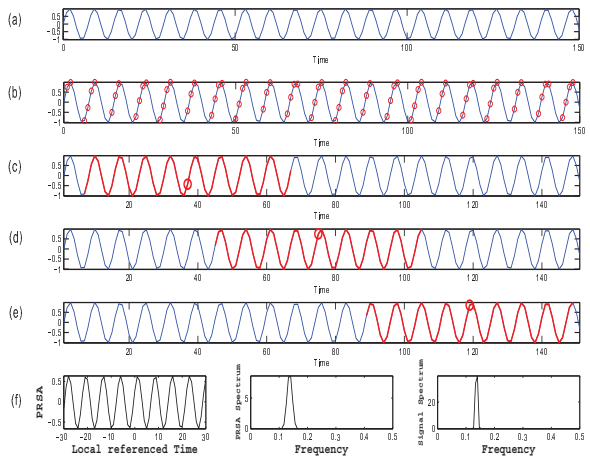

Figure 1: Principle of PRSA: (a) signal $y_n = \sin(2\pi 0.14n)$, (b) Anchor points, (c)-(e) Segments of length $2L+1 = 61$ centered on anchor points, (f) (left side) PRSA signal $\tilde{y}_\ell$ (3), (center) squared modulus of PRSA transform $|\tilde{Y}_q|^2$ (4) and (right side) signal spectrum.

When the signal is corrupted by noise and artifacts, the potential quasi-periodic components which are hidden in a classical Fourier transform of the signal y, appear more clearly using $\tilde{Y}_q$ (4). This is illustrated in Fig.2 for a simulation example. The signal considered is the sum of two sinusoids at frequencies 0.23 Hz and 0.29 Hz. It is contaminated by an additive white Gaussian noise, an impulsive noise and two intermittent frequency modulated components.

As can be observed, the peak frequency at 0.29 Hz is clearly enhanced using the PRSA method (Fig.2(c)) while this peak is hidden in the classical signal spectrum (Fig.2(b)). Other examples illustrating the potential of the PRSA as a tool to improve the estimation of existing periodicities are provided in [12].

2.2 Time frequency representation based on the PRSA

This section re-introduces the PRSA-TFR, which highlights frequency domain events and their time evolution [9]. We

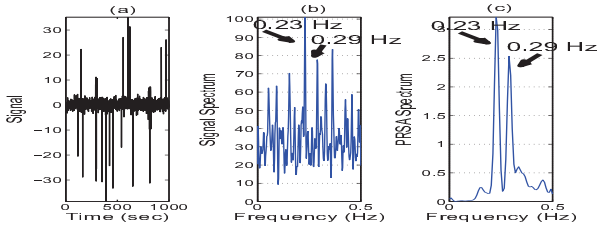

Figure 2: Enhancement of existing quasi-periodic components in signals using PRSA method: (a) studied signal, (b) signal spectrum and (c) squared modulus of PRSA transform $|\tilde{Y}_q|^2$ (4).

examine a signal $\{x_k\}_{k=0,\ldots,K-1}$ by locally applying PRSA over a moving window, with K the total number of samples.

Let us consider a sequence $\{x_{k-K_w+1}, x_{k-K_w+2}, \ldots, x_k\}$ obtained from the signal using a window of length K_w. We denote by $\tilde{x}_{k,\ell}$ the PRSA of this sequence and by $\tilde{X}_{k,q}$ its PRSA transform defined using (3) and (4) by:

$$\tilde{x}_{k,\ell} = \tilde{y}_\ell \quad \text{for } \ell = -L, -L+1, \ldots, L, \qquad (5)$$
$$\tilde{X}_{k,q} = \tilde{Y}_q \quad \text{for } q = 0,1,\ldots,Q-1, \qquad (6)$$

where, for reasons of clarity, the considered sequence is locally named y: $y_n = x_{k-K_w+n}$ for $n = 1,2,\ldots,K_w$.

By repeating the procedure for all $k = K_w,\ldots,K-1$, a time-frequency representation which describes the time-evolution of the PRSA spectrum is obtained in analogy with the short-time Fourier transform and the spectrogram:

$$\begin{array}{ccccc} \text{Time} & \mathbf{x} & \text{Frequency} & \longrightarrow & \text{PRSA-TFR} \\ (k & , & q) & \longmapsto & |\tilde{X}_{k,q}|^2. \end{array} \qquad (7)$$

Figure 3 displays both the PRSA-TFR and spectrogram of the simulated signal of Fig.2(a). One can see that with the PRSA-TFR the impulsive noise level is decreased and the two constant frequencies of the periodic components are enhanced.

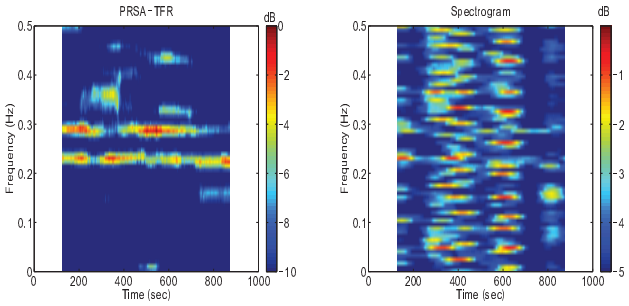

Figure 3: PRSA-TFR (left column) versus spectrogram (right column) of the simulated signal of Fig.2(a).

2.3 PRSA-TFR probability density function

To define the pdf of the PRSA-TFR, we proceed in analogy with that of the spectrogram. In [13, 14], the pdf of spectrogram coefficients obtained by the squared modulus of a discrete Fourier transform is studied. The spectrogram of unit and zero-mean white Gaussian noise, constructed using an infinite rectangular window follows a chi-squared χ^2 law with 2 degrees of freedom.

Let us consider unit and zero-mean white Gaussian noise y,

$y_n \sim \mathcal{N}(0,1)$. The probability distribution of the PRSA $\tilde{y}$ of y can be approximated by (proof in Appendix A):

$$\begin{array}{rcl} \tilde{y}_\ell & \sim & \mathcal{N}\left(0, \frac{1}{\sqrt{M}}\right) \quad \forall\, \ell \in \{-L, -L+1, \ldots, L\} \setminus \{-1, 0\}, \\ \tilde{y}_0 & \sim & \mathcal{N}\left(\frac{1}{\sqrt{\pi}}, \frac{\sqrt{\pi}-1}{\sqrt{M\pi}}\right), \\ \tilde{y}_{-1} & \sim & \mathcal{N}\left(\frac{-1}{\sqrt{\pi}}, \frac{\sqrt{\pi}-1}{\sqrt{M\pi}}\right), \end{array} \tag{8}$$

where M is the number of anchor points. Figure 4 shows the histograms of 20000 simulated samples of $\tilde{y}_{-1}$, $\tilde{y}_{45}$, and $\tilde{y}_0$ for a window length $L = 65$. The approximations (8) (:) are close to the pdfs (-) evaluated using the histograms.

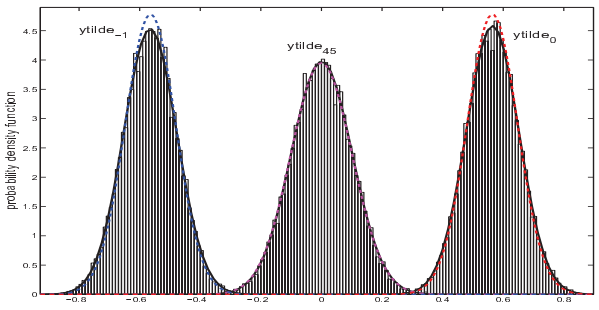

Figure 4: Pdfs of PRSA samples $\tilde{y}_{-1}$, $\tilde{y}_{45}$ and $\tilde{y}_0$. Pdfs obtained by applying PRSA ($L = 65$) to a simulated unit-variance and zero-mean white Gaussian noise. The approximations (8) (:) are superimposed to the pdfs (–) evaluated through simulated samples.

The covariance between the PRSA samples is also approximated by (see appendix A):

$$\begin{cases} Cov(\tilde{y}_{\ell_1}, \tilde{y}_{\ell_2}) = \frac{1}{M\pi}, & \text{if } (\ell_1, \ell_2) = (-1, 0) \text{ or } (0, -1) \\ = 0, & \text{otherwise.} \end{cases} \tag{9}$$

Let us now examine the pdf of the squared modulus of the PRSA transform $S[q] = \left|\tilde{Y}_q\right|^2$ (4). $S[q]$ is written for $Q \geq 2L+1$ as:

$$S[q] = \left|\tilde{Y}_q\right|^2 = S_1^2[q] + S_2^2[q], \quad \text{for } q = 0, \ldots, Q-1, \tag{10}$$

where

$$S_1[q] = \sum_{\ell=0}^{2L} \tilde{y}_{\ell-L} \cos\left(\frac{2\pi q \ell}{Q}\right) \quad \text{and} \quad S_2[q] = \sum_{\ell=0}^{2L} \tilde{y}_{\ell-L} \sin\left(\frac{2\pi q\, \ell}{Q}\right). \tag{11}$$

$S_1[q]$ and $S_2[q]$ are random variables. The closed forms of their means $m_{S_1}[q]$ and $m_{S_2}[q]$ are evaluated using (8) and (9):

$$\begin{array}{rcl} m_{S_1}[q] & = & -\frac{2}{\sqrt{\pi}} \sin\left(\frac{\pi q}{Q}\right) \sin\left(\frac{\pi(2L-1)q}{Q}\right) \\ m_{S_2}[q] & = & \frac{2}{\sqrt{\pi}} \sin\left(\frac{\pi q}{Q}\right) \cos\left(\frac{\pi(2L-1)q}{Q}\right). \end{array} \tag{12}$$

Their variances $\sigma_{S_1}^2[q]$ and $\sigma_{S_2}^2[q]$ are:

$$\begin{array}{rcl} \sigma_{S_1}^2[q] & = & \frac{(2L+1)}{2M}\left[1 + \cos\left(\frac{4\pi qL}{Q}\right)\mathcal{D}(q,L,Q)\right] - \frac{4}{\pi M}\left[\sin\left(\frac{\pi q}{Q}\right)\sin\left(\frac{\pi q(2L-1)}{Q}\right)\right]^2, \\ \sigma_{S_2}^2[q] & = & \frac{(2L+1)}{2M}\left[1 - \cos\left(\frac{4\pi qL}{Q}\right)\mathcal{D}(q,L,Q)\right] - \frac{4}{\pi M}\left[\sin\left(\frac{\pi q}{Q}\right)\cos\left(\frac{\pi q(2L-1)}{Q}\right)\right]^2, \end{array} \tag{13}$$

where $\mathcal{D}(q,L,Q)$ is the Dirichlet kernel function $\mathcal{D}(q,L,Q) = \frac{\sin\left(\frac{2\pi q(2L+1)}{Q}\right)}{(2L+1)\sin\left(\frac{2\pi q}{Q}\right)}$. The covariance coefficient $\rho_{S_1,S_2}[q] = Cov(S_1[q], S_2[q])$ is calculated as:

$$\rho_{S_1,S_2}[q] = \frac{(2L+1)}{2M}\sin\left(\frac{4\pi qL}{Q}\right)\mathcal{D}(q,L,Q) + \frac{2}{\pi M}\left[\sin\left(\frac{\pi q}{Q}\right)\right]^2 \sin\left(\frac{2\pi q(2L-1)}{Q}\right). \tag{14}$$

We indicate that in equations (13) and (14), some terms can be neglected leading to the following simplification:

$$\begin{array}{rcl} \sigma_{S_1}^2[q] & \approx & \frac{(2L+1)}{2M}\left[1 + \cos\left(\frac{4\pi qL}{Q}\right)\mathcal{D}(q,L,Q)\right], \\ \sigma_{S_2}^2[q] & \approx & \frac{(2L+1)}{2M}\left[1 - \cos\left(\frac{4\pi qL}{Q}\right)\mathcal{D}(q,L,Q)\right], \\ \rho_{S_1,S_2}[q] & \approx & 0. \end{array} \tag{15}$$

Figure 5 shows that the theoretical means (12) and variances (13) of both $S_1[q]$ and $S_2[q]$ coincide with the means and variances evaluated on the PRSA of simulated unit-variance and zero-mean Gaussian noise.

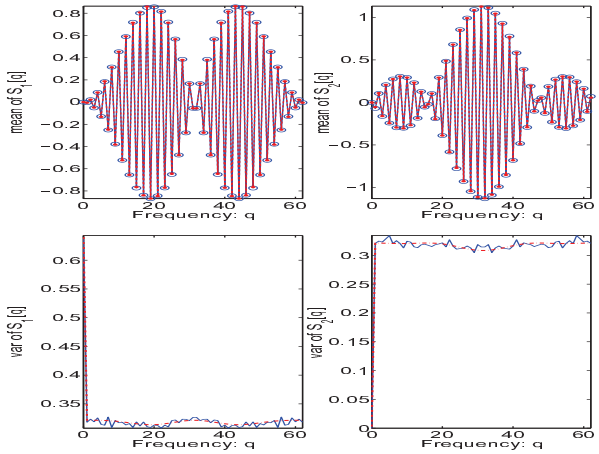

Figure 5: (Top) Theoretical means (12) (–∘) of $S_1[q]$ and $S_2[q]$ coincide with the simulated ones (..•). (Bottom) Theoretical variances (13) (–) of $S_1[q]$ and $S_2[q]$ coincide with the simulated ones (-.-).

In Fig.6, the histograms of both $S_1[q]$ and $S_2[q]$ are illustrated. These histograms are well fitted by Gaussian pdf curves.

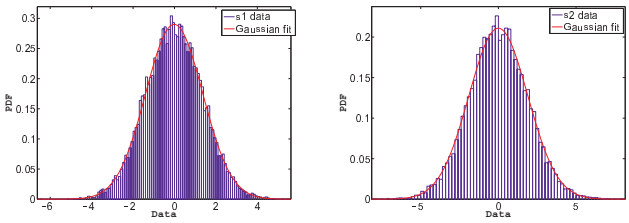

Histogram of $S_1[q]$ Histogram of $S_2[q]$

Figure 6: Pdfs of $S_1[q]$ and $S_2[q]$ (10) illustrated for $M = 100$, $2L+1 = 63$ and $Q = 64$: Gaussian fits (-) are superimposed to the histograms of $S_1[q]$ and $S_2[q]$ which are simulated using unit-variance zero-mean Gaussian noise.

Indeed, according to the strong law of large numbers, both $S_1[q]$ and $S_2[q]$ which are the sum of $2L+1$ samples with $2L+1 \geq 33$, can be assumed to be asymptotically Gaussian random variables:

$$S_1[q] \sim \mathcal{N}(0, \sigma_{S_1}^2[q]) \quad \text{and} \quad S_2[q] \sim \mathcal{N}(0, \sigma_{S_2}^2[q]). \tag{16}$$

By taking into account (15) and (16), and according to [13], the pdf of the squared modulus of the PRSA transform ($S[q] = S_1^2[q] + S_2^2[q]$ (10)) is approximated by:

$$pdf_S\left(\left|\tilde{X}_{n,q}\right|^2 = S[q]\right) = \frac{M}{(2L+1)} \frac{I_0(bS[q])}{\sqrt{1 - \mathcal{D}^2(q,L,Q)}}\, e^{-aS[q]} \tag{17}$$

with $a^{-1} = \frac{(2L+1)}{M}\left(1 - \mathcal{D}^2(q,L,Q)\right)$, $b = a|\mathcal{D}(q,L,Q)|$ and I_0 the zero-order modified Bessel function. This distribution collapses with a χ^2 distribution if $Q = 2L+1$ and for high frequencies (large q):

$$pdf_S\left(\left|\tilde{X}_{n,q}\right|^2 = S[q]\right) = Me^{-MS[q]}, \qquad (18)$$

and for $q = 0$, the $S[q]$ follows a χ^2 law with one degree of freedom [13]: $pdf_S\left(\left|\tilde{X}_{n,0}\right|^2 = S[0]\right) = M\frac{S[0]^{-\frac{1}{2}}}{\sqrt{2\pi}}e^{-M\frac{S[0]}{2}}$.

In the following, we fix $Q = 2L+1$ and hence the pdf of the PRSA-TFR coefficient (7) is assumed to be a χ^2 law (18) with two degrees of freedom [13] for $q \neq 0$. It is also worth noting that pdf_S was theoretically derived for a PRSA-TFR of white Gaussian noise while and other distributions should be more adapted to take into account the overlapping and windowing effects when calculating the PRSA-TFR.

The theoretical windowing and zero-padding effects are studied for the spectrogram in [15], while the case of signal presence (noncentral Gaussian variables) is presented in [14]. Indeed, this last case has no exact pdf formulation and the authors suggest a geometric approach to evaluate the spectrogram pdf. These studies can also be addressed for the PRSA-TFR pdf but this is out of the scope of this paper.

3. HRV DATA SET

This section presents the procedure for generating synthetic HRV signals and specifies the characteristics of the real HRV data.

3.1 Synthetic HRV signals

Realistic synthetic HRV signals at supine and after tilt can be generated using the HRV AR-PSD model described in [8]: $PSD(f) = \frac{\sigma_r^2}{\left|\sum_{k=0}^{p} a_k\ e^{j2\pi f}\right|^2}$. The true model order p, the AR model coefficients a_k and the variance σ_r^2 of the driving zero-mean white noise are reported in Table 1 for a sampling rate of 1 Hz. We add a very low frequency trend, additive white Gaussian noise (AWGN) and impulsive noise to the simulated signals in order to obtain real-like artificial HRV signals.

Table 1: Coefficients and noise variance of the AR models.

Coeff.	a_0	a_1	a_2	a_3	a_4	a_5	a_6	a_7
Supine	1	-1.6265	1.8849	-1.8327	1.2970	-0.7758	0.4133	-0.2136
Tilt	1	-1.8149	2.1365	-2.1703	1.7194	-0.9221	0.5311	-0.3262

	σ_r^2	p
Supine	$404\ 10^{-6}$	7
Tilt	$137\ 10^{-6}$	7

3.2 Real HRV signals

HRV real data are collected from experiments in 11 male cyclists (age 23 (4) years; height 191.1 (3.4) cm; body mass 69.3 (2.5) kg; all values are mean (standard deviation)) during a classical stand-test by means of a Holter device at a sampling frequency equal to 1000 Hz.

4. DISTANCE MEASURE

We propose to evaluate the deviation of the pdf of the PRSA-TFR of HRV recorded during both supine and tilt positions from that of an iid Gaussian noise, the aim being to discriminate HRV changes between both positions based on this deviation. In the following, we describe the steps to measure this deviation. First, we calculate the PRSA-TFR coefficients for the centered and normalized HRV time-series with $Q = 2L+1$ for both positions. We then evaluate the PRSA-TFR pdfs. These pdfs, experimentally obtained, are compared to the pdfs pdf_S (18) using the Battacharya distance. Actually, to evaluate the deviation between two pdfs f_1 and f_2, the Battacharya (B) distance ξ_B is defined by:

$$\xi_B(f_1||f_2) = -\log\left(\int_0^\infty \sqrt{f_1 f_2}\, ds\right). \qquad (19)$$

5. RESULTS AND DISCUSSION

In order to ascertain the potential of the PRSA-TFR, 1000 realizations of realistic artificial HRV signals are initially used for each considered SNR (SNRs are varying from 5 to 30 dB). The results are compared to those obtained by the Yule-Walker AR spectral method, the true model order $p = 7$ being assumed known for this latter method. Both methods are then tested on real HRV data to demonstrate consistency with the simulated results. PRSA-TFR of the (centered and normalized) HRV are evaluated using sliding windows of length $K_w = 100$ and PRSA length $2L+1 = 33$.

Two measurements are evaluated and compared: $\left|\log\left(\frac{Power\ Ratio\ LF/HF_{tilt}}{Power\ Ratio\ LF/HF_{supine}}\right)\right|$ for the Yule-Walker AR spectral method and $\left|\log\left(\frac{\xi_{B\,tilt}}{\xi_{B\,supine}}\right)\right|$ for the PRSA-TFR, ξ_B being defined by (19).

Figure 7 displays the results for the two methods. By comparing these results one can see that for SNR equal 5 and 10 dB the proposed method which contrary to the classical one does not assume fixed spectral bounds, exhibits the same capacity as the classical one. For higher SNR values, the classical method performance is slightly higher than that of PRSA-TFR. However it is important to remind that the classical method performance depends on selecting the appropriate order of the AR model, and here it is assumed to be known. When the minimum description length criterion (MDL) is used to determine the model order [16] before applying the classical method the results worsen.

A deeper performance study of the PRSA-TFR based on the choice of the length L and the sliding window K_w is also important to determine the limitations regarding the PRSA method. This study is out of this paper scope.

6. CONCLUSION AND PERSPECTIVES

In the present paper, we derive the theoretical pdf of PRSA-TFR for Gaussian white noise. The PRSA-TFR is a new time frequency representation based on the PRSA method which allows for detection of the time variation of the most important frequencies in HRV signals. The deviation of the PRSA-TFR pdf of HRV signals during supine and tilt position from that of iid Gaussian noise is measured using the Battacharya distance. This measure helps characterize HRV signals under supine and tilt positions. For instance, this measure does not need to predetermine LF and HF spectral boudaries contrary to classical spectral methods. In future studies, we aim to study the effects of windowing on the PRSA-TFR pdf.

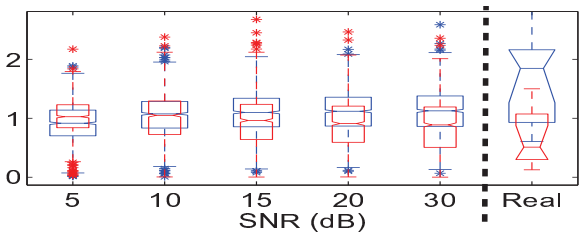

Figure 7: Centered and normalized synthetic and real HRV: results obtained by (blue) Yule-Walker AR spectral method with LF and HF bands defined as 0.04-0.15 Hz and 0.15-0.40 Hz respectively, (red) PRSA-TFR method. PRSA-TFRs are evaluated using a sliding window of length $K_w = 100$ and $2L+1 = 33$ whereas the Yule-Walker AR spectral method is calculated using the true model order $p = 7$. The boxes have lines at the lower quartile, median, and upper quartile values. The whiskers are lines extending from each end of the boxes to show the extent of the supine of the data. Outliers are data with values beyond the ends of the whiskers.

A. DERIVATION OF THE PROBABILITY DENSITY FUNCTION OF PRSA

Let us consider a unit centered Gaussian signal y and its PRSA signal $\tilde{y}_\ell$. Three cases are discussed according to the definition of PRSA (3):

- Case 1 : $\ell \neq \{0,1\}$, $\tilde{y}_\ell$ can be assumed to be a sum of M independent random variables drawn from a unit-variance and zero-mean Gaussian Law. In this case, $\tilde{y}_\ell$ is a Gaussian random variable with zero mean and variance equals $\frac{1}{M}$: $\quad \tilde{y}_\ell \sim \mathcal{N}\left(0, \frac{1}{\sqrt{M}}\right) \quad \forall\, \ell \in [-L,L]\setminus\{-1,0\}$.
- Case 2 : $\ell = 0$, $\tilde{y}_0$ is a sum of M anchor points. The anchor points correspond to increases in thesignal, i.e. instants n defined by (1).
- Case 3 : $\ell = -1$, $\tilde{y}_{-1}$ is a sum of M points occurring just before the anchor points. These M points correspond to the decreases in signal, i.e. instants $n-1$ defined by (1).

To approximate the pdfs of both $\tilde{y}_0$ and $\tilde{y}_{-1}$, we need to examine the pdfs and the statistics of the random variables $Z_1 = y_n$ and $Z_2 = y_{n-1}$ representing the anchor point and the point occurring just before. Since y is a unit and zero-mean Gaussian signal, according to the definition (1), the joint pdf of both Z_1 and Z_2 is written:

$$p_{Z_1,Z_2}(z_1,z_2) = \frac{1}{\pi}\, e^{-\frac{z_1^2+z_2^2}{2}}\, \mathbb{I}_{\{z_2<z_1\}}(z_1,z_2), \tag{20}$$

where $\mathbb{I}_{\{z_2<z_1\}}(z_1,z_2)$ is a function defined by: $\mathbb{I}_{\{z_2<z_1\}}(z_1,z_2) = 1$ if $z_2 < z_1$ and $\mathbb{I}_{\{z_2<z_1\}}(z_1,z_2) = 0$ otherwise. Equation (20) satisfies the probability definition $\int\int p_{Z_1,Z_2}(z_1,z_2)\, dz_1\, dz_2 = 1$. By marginalization of (20), the pdf of Z_1 and Z_2 are obtained:

$$p_{Z_1}(z_1) = \frac{1}{\sqrt{2\pi}}\, e^{-\frac{z_1^2}{2}} \left(1 + erf\left(\frac{z_1}{\sqrt{2}}\right)\right), \tag{21}$$

$$p_{Z_2}(z_2) = \frac{1}{\sqrt{2\pi}}\, e^{-\frac{z_2^2}{2}} \left(1 - erf\left(\frac{z_2}{\sqrt{2}}\right)\right), \tag{22}$$

where $erf(z) = \frac{2}{\sqrt{\pi}} \int_0^z e^{-u^2} du$ is the Gauss error function. The second-order statistics of both of Z_1 and Z_2 are derived using (20), (21) and (22):

$$\begin{aligned} &E[Z_1] = -E[Z_2] = \tfrac{1}{\sqrt{\pi}}; \quad && Var[Z_1] = Var[Z_2] = 1 - \tfrac{1}{\pi}; \\ &E[Z_1 Z_2] = 0; && Cov[Z_1,Z_2] = \tfrac{1}{\pi}. \end{aligned} \tag{23}$$

The definition of PRSA (3) and the statistics (23) allow us to evaluate the second-order statistics of both $\tilde{y}_0$ and $\tilde{y}_{-1}$, by assuming independent anchor points:

$$\begin{aligned} &E[\tilde{y}_0] = -E[\tilde{y}_{-1}] = \tfrac{1}{\sqrt{\pi}}, \quad Var[\tilde{y}_0] = Var[\tilde{y}_{-1}] = \tfrac{\pi-1}{M\pi}, \\ &Cov[\tilde{y}_0,\tilde{y}_{-1}] = \tfrac{1}{M\pi}. \end{aligned} \tag{24}$$

Since we assume both $\tilde{y}_0$ and $\tilde{y}_{-1}$ are the sums of M independent random variables drawn from the pdfs (21) and (22) respectively, the strong Law of Large Numbers can be applied. Both $\tilde{y}_0$ and $\tilde{y}_{-1}$ are then assumed to be Gaussian random variables respectively:

$$\tilde{y}_0 \sim \mathcal{N}\left(\tfrac{1}{\sqrt{\pi}}, \tfrac{\sqrt{\pi-1}}{\sqrt{M\pi}}\right) \quad \text{and} \quad \tilde{y}_{-1} \sim \mathcal{N}\left(\tfrac{-1}{\sqrt{\pi}}, \tfrac{\sqrt{\pi-1}}{\sqrt{M\pi}}\right). \tag{25}$$

We remind $\tilde{y}_0$ and $\tilde{y}_{-1}$ are correlated random variables, so their covariance is different from zero (24).

REFERENCES

[1] J. Gross, L. Carstensen, M. P. M, J. Tsai, C. S. CG, A. Hsu, Emotion and aging: experience, expression, and control, Psy. Aging 12(4) (1997) 590–599.

[2] Q. Liu, C. Poon, Y. Zhang, Time-frequency analysis of variabilities of heart rate, systolic blood pressure and pulse transit time before and after exercise using the recursive autoregressive model, Biomed. Sig. Proc. and Control 6(4) (2011) 364–369.

[3] T. F. of The European Society of Cardiology, T. N. A. S. of Pacing, Electrophysiology, Heart rate variability, European Heart Journal 17 (1996) 354–381.

[4] R. D. Berger, S. Akselrod, D. Gordon, R. J. Cohen, An efficient algorithm for spectral analysis of heart rate variability, IEEE Trans. on Biomed. Eng. (1986) 900–904.

[5] G. D. Clifford, L. Tarassenko, Quantifying errors in spectral estimates of HRV due to beat replacement and resampling, IEEE Trans. on Biomed. Eng. 52 (2005) 630–638.

[6] Y. Goren, L. R. Davrath, I. Pinhas, E. Toledo, S. Akselrod, Individual time-dependent spectral boundaries for improved accuracy analysis of heart rate variability, IEEE Trans. on Biomed. Eng. 53 (2006) 35–42.

[7] J. W. Kantelhardt, A. Bauer, A. Y. Schumann, P. Barthel, R. Schneider, M. Malik, G. Schmidt, Phase rectified signal averaging for the detection of quasi periodicities and the prediction of cardiovascular risk, CHAOS 17 (2007) 015112.

[8] J. Mateo, P. Laguna, Improved heart rate variability signal analysis from the beat occurrence times according to the IPFM model, IEEE Trans. on Biomed. Eng.j 47:8 (2000) 985–996.

[9] M. Jabloun, J. V. Zaen, J. M. Vesin, Time-frequency analysis based on the phase-rectified signal averaging method, in: 17th EUSIPCO, Glasgow, 2009.

[10] A. Bauer, J. Kantelhardt, A. Bunde, P. Barthel, R. Schneider, M. Malik, G. Shmidt, Phase rectified signal averaging detects quasi-periodicities in non-stationary data, Physica A 364 (2006) 423–434.

[11] M. Daoud, P. Ravier, M. Jabloun, B. Yagoubi, O. Buttelli, Estimation of spectral parameters of nonstationary hrv signals using gaussian fitting spectra, in: ISABEL, 2011.

[12] M. Lemay, Y. Prudat, V. Jacquemet, J. Vesin, Phase rectified signal averaging used to estimate the dominant frequencies in ECG signals during atrial fibrillation, IEEE Trans. on biomed. Eng. 55 (2008) 2538 – 2547.

[13] T. Durrani, J. Nightingale, Probability distributions for discrete Fourier spectra, Proc. Inst. Elec. Eng. 120 (1973) 299–311.

[14] J. Huillery, F. Milloz, N. Martin, On the description of spectrogram probabilities with a chi-squared law, IEEE Trans. on SP 56 (2008) 2249–2258.

[15] T. Durrani, Joint density functions for digital spectra, IEEE Trans. ASSP 22 (1974) 314–320.

[16] D. MacKay, Information Theory, Inference, and Learning Algorithms, Cambridge University Press, 2003.